THE ROYAL SOCIETY

Evanescent-wave microscopy: a new tool to gain insight into the control of transmitter release

Martin Oheim[1,2], Dinah Loerke[1], Robert H. Chow[2] and Walter Stühmer[1]

[1]*Max-Planck Institute for Experimental Medicine, Department of Molecular Biology of Neuronal Signals, Hermann-Rein Strasse 3, D-37075 Göttingen, Germany* (*oheim@mail.mpiem.gwdg.de, loerke@mail.mpiem.gwdg.de, stuhmer@mail.mpiem.gwdg.de*)
[2]*Department of Physiology, University of Edinburgh Medical School, Membrane Biology Group, Teviot Place, Edinburgh EH8 9AG, UK* (*robert.chow@ed.ac.uk*)

Evanescent-wave excitation was used to visualize individual fluorescently labelled vesicles in an optical slice near the plasma membrane of bovine adrenal chromaffin cells. A standard upright microscope was modified to accommodate the optics used for directing a laser beam under a supracritical angle on to the glass–water interface on top of which the cells are grown. Whereas epi-illumination images appeared blurred and structureless, evanescent-wave excitation highlighted acridine orange-labelled vesicles as individual pinpoints. Three-dimensional (3D) trajectories of individual vesicles were obtained from time-resolved image stacks and used to characterize vesicles in terms of their average fluorescence F and mobility, expressed here as the 3D diffusion coefficient $D^{(3)}$. Based on the single-vesicle analysis, two groups of vesicles were identified. Transitions between these states were studied before and after stimulation of exocytosis by repetitive or maintained membrane depolarizations by elevated extracellular $[K^+]$. Findings were interpreted as sequential transitions between the previously characterized pools of vesicles preceding the fusion step. The observed approach of vesicles to their docking sites was not explained in terms of free diffusion: most vesicles moved unidirectionally as if directed to their binding sites at the plasma membrane. Vesicle mobility at the membrane was low, such that the sites of docking and fusion were in close vicinity. Both the rim region and confined areas in the centre of the footprint region were the site of intense vesicle trafficking.

Keywords: total internal reflection; evanescent-wave microscopy; optical sectioning; Ca^{2+}-triggered exocytosis; diffusion; docking

1. INTRODUCTION

Vesicle transport and maturation steps preceding membrane merger and release of transmitter or hormones play an important role in regulating the rate of secretion (Augustine & Neher 1992; Rüden & Neher 1993). Until recently (Steyer *et al.* 1997; Oheim *et al.* 1998*a*), no direct studies of the intracellular translocation, docking and transitions leading towards exocytosis had been possible. Indirect insight was gained from studying the depression of the secretory response by repetitive or maintained stimulation (Elmquist & Quastel 1965; Betz 1970; Stevens & Tsujimoto 1995; Rosenmund & Stevens 1996). By measuring the recovery of the rate of release from previous stimuli (Moser & Neher 1996; Gillis & Chow 1997; Smith *et al.* 1998) the time-course of depletion and refill of a near-membrane pool of release-ready vesicles was estimated (Bittner & Holz 1992; Ammala *et al.* 1993; Gillis & Misler 1993; Horrigan & Bookman 1994).

2. EXPERIMENTAL APPROACHES TO STUDY SECRETION

Three main approaches have been used to study exocytosis from single cells:

(i) capacitance measurements that trace changes of the cell surface area due to membrane addition by fusion of secretory vesicles;
(ii) electrochemical detection by oxidation or reduction of released transmitter molecules at the surface of a carbon-fibre electrode placed in close vicinity of the site of release;
(iii) optical techniques monitoring release, membrane addition or pH changes.

See Angleson & Betz (1997) and Neher (1998) for recent reviews of these methods.

(a) *Capacitance measurements of the cell surface area*

Vesicle fusion and membrane re-uptake during exocytosis and endocytosis lead to an increase or decrease in the cell surface area and, correspondingly, in the cell's membrane capacitance (C_m) (Neher & Marty 1982). Patch clamp measurements (Hamill *et al.* 1981) of secretion rely on these changes in C_m. Different techniques used for estimating C_m have recently been reviewed (Gillis 1994). One problem associated with dC_m measurements is that they only report net changes: reliable estimates of the rate of secretion are only obtained if exo- and endocytosis are clearly separable.

 © 1999 The Royal Society

(b) *Amperometric detection of released molecules*

Electrochemical detection is based on the oxidation or reduction of released transmitter molecules (Wightman *et al*. 1991; Chow *et al*. 1992). The oxidation current is a direct measure for release and—unlike C_m—is not model-dependent. Still more importantly, it is not susceptible to interference from endocytosis. The cell is not subject to whole-cell dialysis and wash-out of diffusible cytoplasmic constituents. Stimulation of the cell leads to a shower of spiking oxidative transients, sometimes preceded by a small pedestal signal, indicative of transmitter trickling from the fusion pore—a water-filled channel that initiates the connection between vesicle interior and cell exterior (Almers 1990). Single fusion events have been studied using an electrochemical electrode inside a patch pipette, an approach called patch-amperometry (Albillos *et al*. 1997).

(c) *Optical methods to study secretion*

High-resolution differential interference contrast (DIC) microscopy has been used to visualize single secretory events in chromaffin cells (Terakawa *et al*. 1991). In DIC, the high refractive-index difference between the granular matrix and the cytoplasm generates sufficient contrast to highlight vesicles. Other techniques have used fluorescent labels to generate contrast.

(i) *Monitoring ATP-release*

In many types of secretory cells vesicles contain adenosine-5′-triphoshate (ATP) in addition to the transmitters or hormones. ATP release can be monitored using the luciferase-catalysed luminescent oxidation of luciferin (Biggley *et al*. 1967; Rojas *et al*. 1986, 1990). The light level only permitted a photometric assay of secretion on populations of chromaffin cells with a time resolution in the order of seconds.

(ii) *Endocytotic uptake of amphiphilic dyes*

Real-time optical monitoring of synaptic vesicle recycling in isolated cells was made possible with the advent of styryl dyes (Betz & Bewick 1992; Betz *et al*. 1992). These dyes partition into lipid membranes and become trapped in recycled vesicles on endocytosis. Further stimulation of synaptic transmission causes preloaded vesicles to release dye into the bathing medium, and fluorescence thereby declines (Betz *et al*. 1996; Betz & Angleson 1997). Instead of labelling the vesicular membrane, the vesicular contents can be made fluorescent. Using this technique in combination with C_m measurements, exo- and endocytosis were simultaneously measured (Smith & Betz 1996).

(iii) *Labelling of vesicles with acidotropic dyes*

Several cationic monoamines or diamines can move freely across membranes in their unprotonated form and will accumulate in the protonated form inside the vesicle, which has a lower pH (*ca*. 5.5) compared with the cytosol (*ca*. 7.2). These include acridine orange (Wall *et al*. 1994), quinacrine and dyes of the lysotracker–lysosensor families (Diwu *et al*. 1994; Zhang *et al*. 1994). Unfortunately, these dyes label other acidic compartments, such as endosomes and lysosomes, as well, such that fluorescence may originate from non-vesicular organelles.

(iv) *Green fluorescent protein*

More specific staining of secretory organelles was achieved by using variants of the green fluorescent protein (GFP) of the jellyfish *Aequorea victoria*. When linked to the vesicular protein chromogranin A and expressed in cells, it retains its fluorescence properties and can therefore be used as a vesicle marker (Kaether & Gerdes 1995; Lang *et al*. 1997; Wacker *et al*. 1997). Like the acidotropic dyes, it is released with the vesicular contents after membrane merger such that exocytosis is observed as a decrease in fluorescence. Recently, pH-dependent GFP mutants have become available (Miesenböck *et al*. 1998).

3. LIMITATIONS OF PRESENT TECHNIQUES

Although both capacitance and electrochemical techniques allow measurements of single-vesicle fusion in chromaffin cells to be performed with millisecond-time resolution, these techniques suffer from two major drawbacks:

(i) their spatial resolution is low (as with whole-cell C_m-measurements or large-diameter carbon fibre electrodes with 5–8 μm tip diameter) or else punctual (as with on-cell C_m-measurements (Henkel 1998) or patch-amperometry (Albillos *et al*. 1997));
(ii) they do not provide information on the steps prior to membrane fusion or after endocytotic uptake of membrane since they measure membrane addition or release, respectively.

In principle, existing imaging techniques could be used to address these questions but have suffered from several limitations that have limited their application to studies of secretion:

(i) the temporal resolution of optical approaches is limited by the time needed to collect enough photons, and beam-scanning is slow compared to the time-scale of vesicle fusion;
(ii) out-of-focus signal causes small neighbouring structures to blur into one patch such that single vesicles are not resolved;
(iii) single-vesicle arrival or fusion events are not detected since fluorescence changes only constitute a small fraction of the total signal.

4. TAILORING FLUORESCENCE MICROSCOPY TO THE NEEDS OF SINGLE-VESICLE OBSERVATION

Reducing the volume fraction of the cell in which fluorescence is excited will increase the relative change in fluorescence. Due to their effective suppression of out-of-focus light (Agard *et al*. 1989; Hiraoka *et al*. 1990), confocal microscopy (Minsky 1961, 1988; Pawley 1995) and multiphoton excitation fluorescence microscopy (Denk *et al*. 1990, 1996; Lipp & Niggli 1993; Piston *et al*. 1994; Svoboda *et al*. 1996) achieve a confinement of light collection or excitation to a small volume. Indeed, an application of three-photon excitation to measure the serotonin content of granules in living cells has been reported (Maiti *et al*. 1997). But until recently, slow image acquisition rates have limited the use of scanning microscopes in studies of single-vesicle dynamics (Burke *et al*.

1997; Neher *et al.* 1998). The limited spatial resolution of conventional wide-field optics, particularly along the optical axis of the microscope, makes it difficult to resolve individual vesicles out of a blur of densely packed vesicles inside a cell. DIC and fluorescence microscopy were used to study vesicles prior to exocytosis (Terakawa *et al.* 1991; Betz *et al.* 1996; Maiti *et al.* 1997; Ryan *et al.* 1997) but these studies have lacked the spatial resolution to resolve individual vesicles out of a blur of fluorescence (Betz & Bewick 1992; Smith & Betz 1996).

5. EVANESCENT-WAVE MICROSCOPY

Direct monitoring of individual near-membrane vesicles has become possible with the introduction of evanescent-wave microscopy (Axelrod *et al.* 1992) to studies of secretion (Lang *et al.* 1997; Steyer *et al.* 1997; Oheim *et al.* 1998*a*). Evanescent-wave excitation of fluorescence is based on the decaying near-field generated near a dielectric interface on the total internal reflection of light. Due to the exponential decay of the evanescent field, total internal reflection fluorescence microscopy (TIRFM) achieves its highest sensitivity very close to a dielectric interface. Thus, it lends itself in a natural way to investigations of surface topography, film thickness, refractive index and absorption close to interfaces.

(a) *Generation of evanescent waves by total internal reflection*

Light incident on a dielectric interface (from a higher to a lower refractive index medium) at a supracritical angle $\theta_{i,c}$ (defined by Snell's law) is totally reflected back into the higher refractive index medium (figure 1). An exponentially decaying evanescent field is created in the lower index medium. The exponential decay constant d of the evanescent field intensity $I(z)$ is typically 30–300 nm and depends on media refractive indices, incidence angle and illumination wavelength.

$$I(z) = I(0)\exp(-z/d), \tag{1}$$

where the decay length

$$d = \frac{1}{2k\sqrt{\sin\theta_i/\sin\theta_{i,c})^2 - 1}} = \frac{\lambda_0}{4\pi\sqrt{n_1^2\sin^2\theta_i - n_2^2}} \tag{2}$$

is a function of the refractive indices, n_1 and n_2, respectively, the angle of incidence θ_i and the wavelength λ_0.

The intensity of the evanescent wave-field at the interface, $I(0)$ is calculated by coherent superposition of the incident and reflected beam and solving Maxwell's equations for the appropriate boundary conditions. It depends on the angle of incidence, the refractive indices and the electric field amplitude A (Born & Wolf 1980). For *s*-polarized light,

$$I_s(0) = |A_s|^2 4\cos^2\theta_i/(1 - n_2^2/n_1^2), \tag{3}$$

and for *p*-polarized light

$$I_p(0) = |A_p|^2 \frac{4\cos^2\theta_i(2\sin^2\theta_i - n_2^2/n_1^2)}{(n_2/n_1)^4\cos^2\theta_i + \sin^2\theta_i - n_2^2/n_1^2}. \tag{4}$$

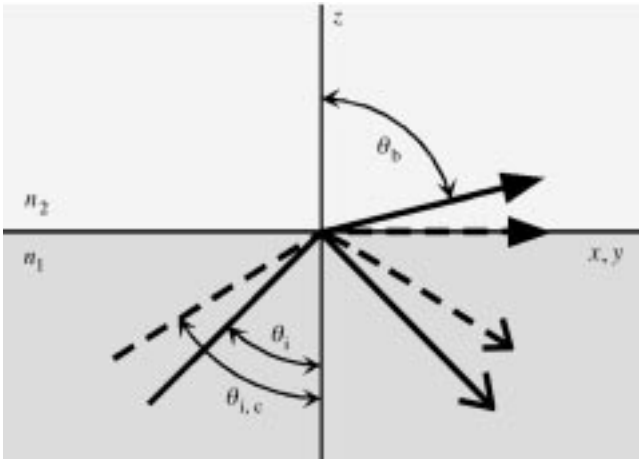

Figure 1. Refraction and reflection of light at a dielectric interface. Light incident at an interface (n_1/n_2, where $n_1 > n_2$) is refracted according to Snell's law: $\sin\theta_i/\sin\theta_b = n_2/n_1$, until total internal reflection occurs at the critical angle, $\theta_{i,c} = \sin^{-1}(n_2/n_1)$. Evanescent waves that penetrate only a fraction of the wavelength of light into the medium with refractive index n_2 occur for angles $\theta_i > \theta_{i,c}$. The evanescent wave-field decays exponentially with increasing distance z from the interface.

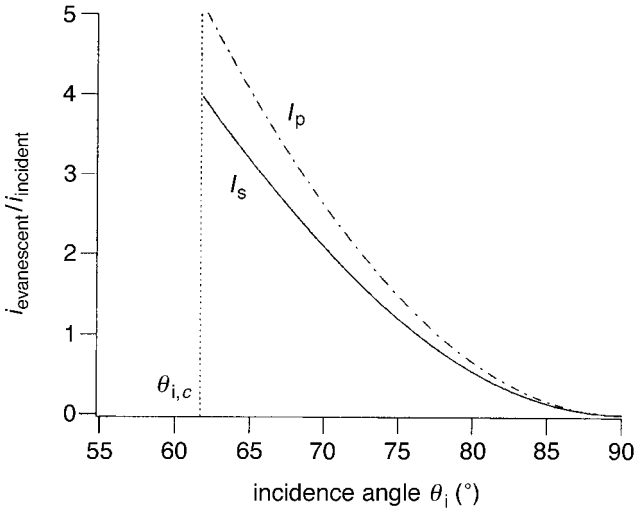

Figure 2. Intensity of the evanescent wave at the interface for linearly polarized light with a polarization angle parallel to the plane of incidence (I_p) and perpendicular (German: 'senkrecht', I_s). Note the 'surface enhancement' of the evanescent intensity at the interface that can be severalfold that of the incident light.

6. METHODS

Two different optical configurations have been used to ensure supracritical beam incidence to the dielectric interface:

(i) a 'prismless' inverted geometry (figure 3) where the beam is guided to the interface through the periphery of a high-numerical aperture (NA)-objective of a standard inverted microscope (Stout & Axelrod 1989; Conibear & Bagshaw 1996; Steyer *et al.* 1997);

(ii) an upright microscope, where the additional condenser optics is located opposite the objective lens (figure 4). In the present set-up, a half-cylindrical prism guides the

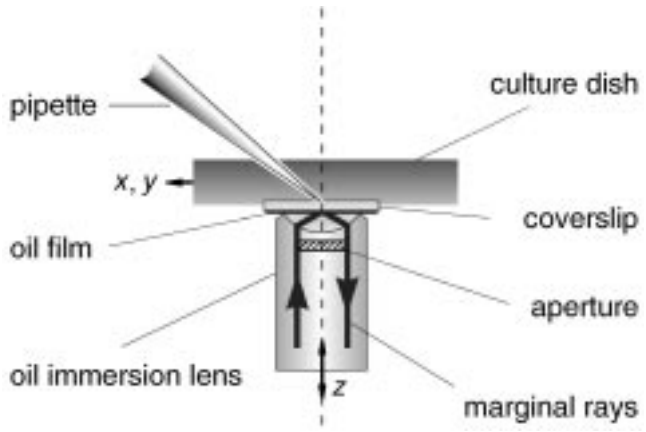

Figure 3. General layout of the prismless evanescent-wave microscope. An inverted microscope is modified such that only light at an angle larger than the critical angle hits the interface. Supracritical beam incidence is ensured by blocking a central region of the optical path so that only marginal rays illuminate the specimen, corresponding to an NA > 1.341. Thus, inverted microscopes with oil immersion lenses of NA 1.4 have been used for this type of evanescent-wave excitation. Incidence angles are fixed and are given by the NAs between 1.341 and the effective NA—that will in practice be <1.4. The penetration depth is $d = \lambda_0/4\pi\sqrt{NA_{\text{eff}}^2 - n_2^2}$ and ranges between about 200 and 300 nm. Reported values are slightly higher, most likely due to scattered light at the inside of the objective's periphery (a detailed description is found in Stout & Axelrod (1989)).

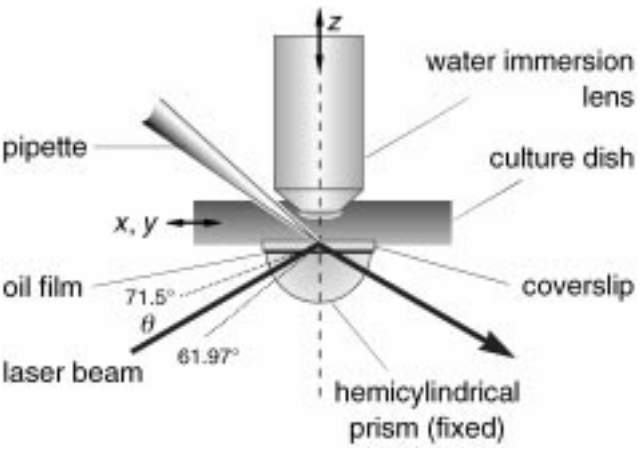

Figure 4. Schematic of the prism approach of VA-TIRFM. The prism approach decouples the excitation and collection pathway. The water immersion objective is located opposite the reflecting interface. Cells are placed in glass-bottomed holders that are coupled to the prism using low-fluorescence index-matched immersion oil. Prism and objective are fixed and centred to the optical axis whereas the chamber slides in the (x, y) plane on a thin oil film. A piezo-electric device enables accurate focusing to the interface layer. This layout allows for evanescent excitation at multiple angles of incidence. In practice, numerical apertures are limited to 1.2 (see Oheim *et al.* (1998) for details). (Modified from Oheim *et al.* (1998*a*).)

beam to the reflecting interface (Oheim *et al.* 1998*a*,*b*). This geometry is particularly favourable if images are taken at multiple angles of incidence.

(a) *The 'prismless' method for fixed-angle TIRFM*

High-NA oil-immersion objectives with $NA > n_2$ allow epi-illumination at supracritical angles of incidence. In this approach, only the peripheral rays are used for fluorescence excitation (Stout & Axelrod 1989). Light travelling closer to the optical axis (corresponding to lower numerical apertures) is incident at angles below the critical angle and penetrates into the object. Therefore, an appropriately sized opaque disk is placed in the objective's back focal plane (BFP) that blocks all but the marginal rays with $NA > n_2$. However, this aperture would also block a fraction of the collected emission light and—for all available high-NA lenses—had to be located inside the objective body. The existence of conjugate planes in the excitation pathway allows one to arrive at the same result by placing an equivalently sized aperture in the equivalent back focal plane (EBFP). This creates a real-image shadow of the disk at the location of the BFP. In the present setup, an achromatic doublet ($f = 110$ mm) is used to generate a 1:1 map of the annular aperture. The ring has an outer diameter of 4.5 mm and a width of *ca.* 100 μm. The aperture is placed at the EBFP on a three-axes manipulator. The light source is located in a conjugate plane of the object plane of the Zeiss 100× 1.4 oil Plan Apochromat objective lens ('critical illumination') such that irregularities in the beam profile show up in the excitation light's intensity distribution. The details of this approach are outlined in Stout & Axelrod's original work for non-infinity optics. The optical path simplifies for infinity-corrected microscopes (Conibear & Bagshaw 1996). Unlike the 'prism-approach' (see below) the prismless microscope in its simple form lacks the possibility to perform θ-scans (Lanni *et al.* 1985; Reichert *et al.* 1987; Suci & Reichert 1988; Burmeister *et al.* 1994; Oheim *et al.* 1998*b*,*c*).

(b) *The 'prism-technique' allows beam incidence at variable angles*

Due to its ability to control the angle of incidence and as a consequence (see equation (2)) modulate the decay length of the evanescent field, the 'prism approach' (figure 4) was given preference for most experiments presented in this study. A laser beam was guided at a supracritical angle onto the cell–substrate interface by shining it on the curved surface of a hemicylindrical BK-7 prism. The flat top of the prism was optically coupled to the fixed glass bottom of the recording chamber by a thin layer of index-matched immersion oil. The centre of symmetry for the entire system was the midpoint of the flat top of the hemicylindrical prism, at which the laser beam was aimed at all times, regardless of the angle of incidence. The microscope, prism and laser optics were moved together as a unit, relative to a fixed stage, on which were located the recording chamber and the micromanipulators used to hold the patch clamp headstage and pipette, application pipette and amperometric detection electrode. A description of the technical detail of this microscope is published elsewhere (Oheim *et al.* 1998*a*,*b*).

Due to the larger angle θ_i attainable, the prism approach achieves a better optical sectioning. Furthermore, the ability to introduce systematic variations of the beam angle and thereby control the penetration depth of the evanescent field offers an additional advantage when a quantitation of fluorescence intensities is desired.

(c) *Estimation of the penetration depth of the evanescent wave* in vivo

Evanescent-wave excitation can provide quantitative information about fluorophore location and concentration near the

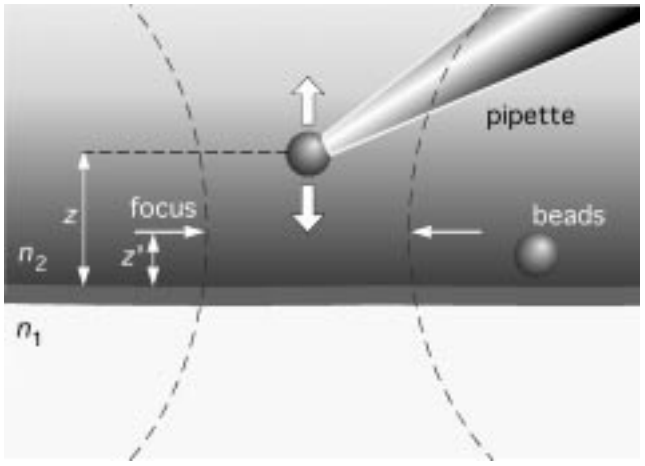

Figure 5. Probing the near-field. Dye-labelled 100- and 200-nm latex microspheres ('beads', Molecular Probes, Eugene, OR, USA) were held at the tip of very pointed glass pipettes. The bead's distance from the reflecting interface was varied with a piezo-electric manipulator. To measure the vertical distance z between the bead and the glass surface, the intensity maximum in a stack of images acquired at different focal planes, z', was determined. The spacing was calculated from the calibrated voltage of the piezo-electric focus drive. The position of the reflecting interface was determined similarly from the maximum-intensity plane of beads dispersed on the interface (see Oheim *et al*. (1999) for details).

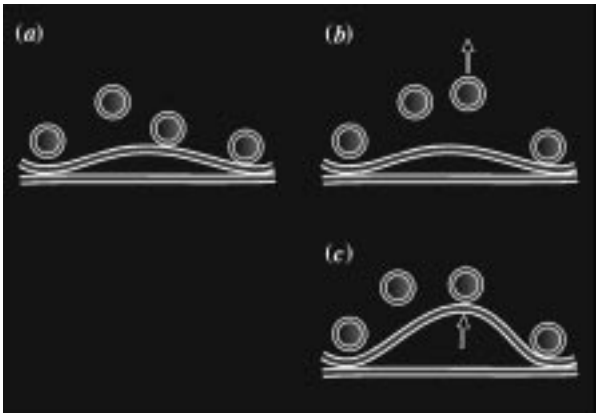

Figure 6. Complications in the interpretation of TIRF images. (*a*) TIR occurs at the top of the glass coverlip ($n_1 \approx 1.52$), irrespective of the precise refractive index of the lower index medium, n_2, as long as $n_2 < n_1$. A decrease in fluorescence intensity of a vesicle that is observed in a time-resolved image stack could be due to (*b*), the withdrawal of the vesicle from the membrane or else (*c*), the buckling up of the membrane while the membrane–vesicle separation distance remains the same. Thus, dynamic alterations of the cell–substrate contact region that can occur during experiments, particularly after long observation periods, solution exchange or during whole-cell dialysis, result in fluorescence changes that are hard to interpret.

reflecting interface (Axelrod 1981; Burghardt & Thompson 1984*a*,*b*; Gingell *et al*. 1987; Reichert *et al*. 1987; Suci & Reichert 1988; Truskey *et al*. 1992; Burmeister *et al*. 1994; Farinas *et al*. 1995; Li & Xie 1996; Swaminathan *et al*. 1996; Chiu *et al*. 1997; Ölveczky *et al*. 1997). To quantify fluorescence intensities, the distribution of excitation light as well as the light collection properties of the objective must be known. The decay length of the evanescent wave, d, specifies the distance from the reflecting interface at which the light intensity of the near-field is attenuated to $1/e$ of its value at the interface (equation (1)). The amount of signal is determined by the decay length as well as the amount of unwanted fluorescence excited distal from the interface. Therefore, we verified the decay of the evanescent field intensity experimentally.

(d) *Probing the near-field*

Fluorescently labelled mircospheres, attached to the tip of a patch pipette were positioned at different distances from the reflecting interface to probe the near-field (figure 5). Keeping the beam angle fixed, the fluorescence of a bead at different distances from the reflecting interface was measured. Plotting the ratio $F/F_{\max}$ versus distance a confirmed the calculated mono-exponential decay of the fluorescence signal with increasing distance from the reflecting interface (not shown, see Oheim *et al*. (1998*a*) for details).

Probing the evanescent field at different (x, y) positions in the elliptical region did not reveal different decay lengths. This is expected since the cone angle of the focused beam is small. During initial experiments, a non-evanescent light component was measured that contributed 1.6% to the signal measured at the interface. Light scattering and reflections at intermediate optical surfaces as well as the back-reflection at the glass–air interface where the reflected beam leaves the prism caused not only interference but also light incident at subcritical angles.

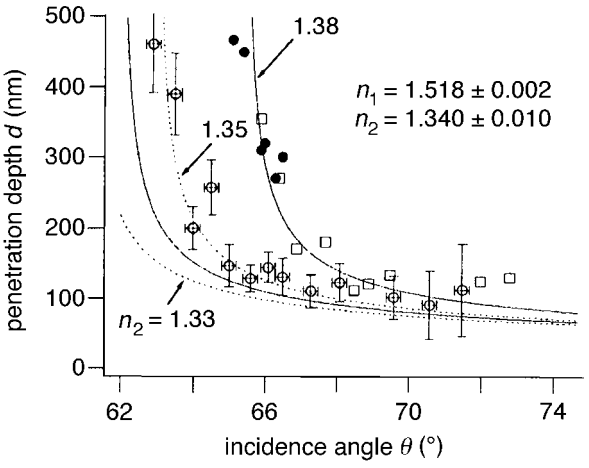

Figure 7. Penetration depth $d(\theta; z)$ as a function of the angle of incidence. Calculated values (solid line) and measured values (open circles) for the $1/e$ decay length of the evanescent field at a BK-7–solution interface ($n_1 = 1.34$). In practice, values for the cytoplasm's refractive index vary between 1.33 and 1.35 allowing d to be predicted only within the dotted lines. Solid dots represent the data obtained when fluorescent beads were sprinkled over a red blood cell ghost. Open boxes indicate measured decay lengths from experiments, in which a bead was pushed through the upper membrane of a chromaffin cell and its fluorescence was measured intracellularly. Data were best described when the cytoplasm was assumed to have a homogeneous refractive index of 1.38, i.e. when the *in vitro* data was scaled with a factor of *ca*. 1.03.

Anti-reflection coating and a beam trap (Oheim *et al*. 1998*b*) completely eliminated this non-evanescent component.

The decay of the evanescent field was measured at the interface between BK-7 glass ($n_1 = 1.552$) and aqueous solution. Bovine serum albumin was added to increase the refractive

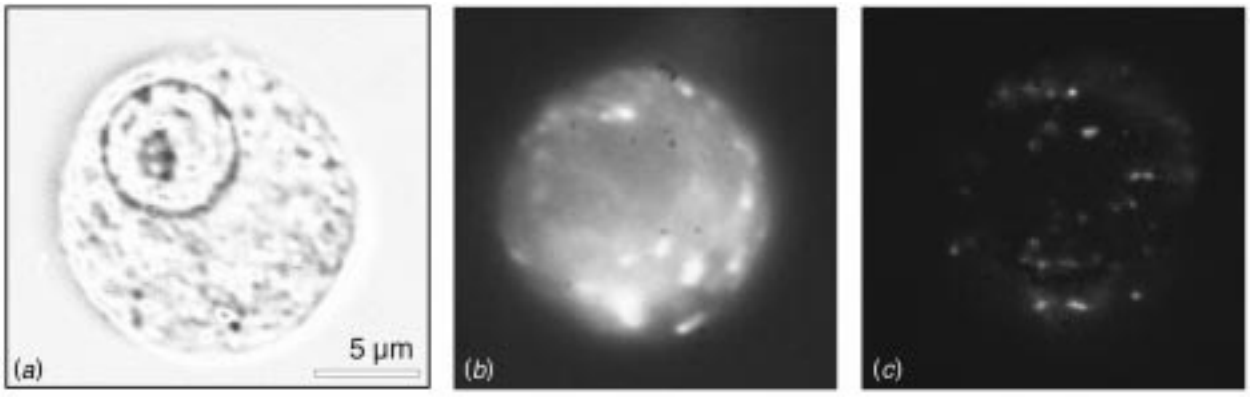

Figure 8. Images of a chromaffin cell. (*a*) Bright field transmission image taken with the Zeiss 100× 1.0w Achroplan, the scale bar is 5 µm. (*b*) Epi-fluorescence excitation image of the same cell loaded with acidotropic fluorescent dye, excited at 488 nm. The image appears blurred and structureless such that no single vesicles can be resolved. (*c*) The evanescent-wave excitation image of the same cell reveals punctate fluorescence. (The cell was pre-incubated in 40 nM lysotracker green added to the cell culture medium 30 min before the experiment. The penetration depth of the evanescent wave was 261 ± 39 nm. Laser intensity was *ca.* 0.65 mW post-fibre.) (Modified from Oheim *et al.* (1998*a*).)

index to n_2=1.35. The angle of incidence was now varied while the bead–substrate separation distance was kept fixed (figure 7). The results followed the calculated curve (equation (2)) for the glass–solution interface (n_2=1.35, solid line). At larger angles (corresponding to smaller penetration depths), the measured intensities slightly exceeded the calculated one and the SNR decreased, because the fluorescence signal decreased while the camera noise remained constant.

7. AMBIGUITIES IN THE INTERPRETATION OF FLUORESCENCE DATA

The knowledge of the penetration depth of the evanescent wave does not remove the ambiguities in the interpretation of evanescent-wave fluorescence images of vesicles in cells, for the following reasons:

(i) cells do not make a flat contact with the substrate they grow on but show focal adhesion sites (Gingell *et al.* 1985; Reichert & Truskey 1990; Truskey *et al.* 1992; Burmeister *et al.* 1994). However, TIR will occur at the glass–water interface rather than at the functionally relevant cell–water interface such that the reflecting interface rather than the plasma membrane is the plane of reference for distance measurements (figure 6);
(ii) the decay of the evanescent wave is modified by the higher-refractive index medium of the cytoplasm compared to aqueous solution, resulting in local modifications of the penetration depth (Gingell & Todd 1979; Gingell *et al.* 1987; Ölveczky *et al.* 1997).

A standard technique used to remove this ambiguity—interference reflection microscopy (IRM) (Curtis 1964; Gingell & Todd 1979)—is not easily combined with the prism approach. In IRM, contrast is generated by constructive or destructive interference of two monochromatic light rays, one reflected at the glass–water interface, the other at the water–cell interface.

(a) *Cells modify the evanescent field*

Penetration depths measured from beads sprinkled over the flat cell body of a red blood cell ghost were larger than those obtained in the case of the bare glass–water interface (figure 7, solid dots). Values for bead–interface distances closer than 270 nm could not be obtained, indicating the minimum thickness of the red blood cell ghost. Therefore the fluorescence of a dye-labelled bead was measured inside a chromaffin cell. A bead, firmly glued to the pipette tip, was pushed through the plasma membrane and its intracellular fluorescence measured. The measured penetration depths were comparable with those obtained when beads were dispersed on top of the blood cell (figure 7, open boxes). Plotting d versus θ_i, the measured values were best described when a (homogeneous) cytosolic refractive index of $n_2 \approx 1.38$ was assumed.

(b) *Spots represent individual vesicles*

Chromaffin cells (figure 8*a*) were incubated with acidotropic dyes. Conventional epi-illumination images appeared blurred and structureless (figure 8*b*). After switching to evanescent-wave excitation, images displayed punctuate fluorescence with almost no background (figure 8*c*). Identification of single vesicles under evanescent-wave excitation was ascertained by demonstrating that four different requirements are being met by the observed spots (Steyer *et al.* 1997; Oheim *et al.* 1998*a*). As single secretory granules: (i) they were of the right size and number density; (ii) they disappeared on secretagogue application, coincident with a small cloud of released fluorescent dye serving as a convenient criterion for monitoring release; (iii) furthermore, maintained stimulation led to the disappearance of spots, with kinetics appropriate to the exhaustion of the releasable pool of granules (Gillis *et al.* 1996). Additionally, manoeuvres that block exocytosis blocked the disappearance of the spots; (iv) finally, as shown for synapses (DelCastillo & Katz 1954) and chromaffin cells (Chow *et al.* 1992) the number of vesicles released on submaximal stimulation followed Poisson statistics. Additional evidence confirming the visualization of individual fusion events came from the combined use of evanescent-wave microscopy and capacitance measurements (M. Oheim and D. Loerke, unpublished data) and amperometry (Steyer *et al.* 1997).

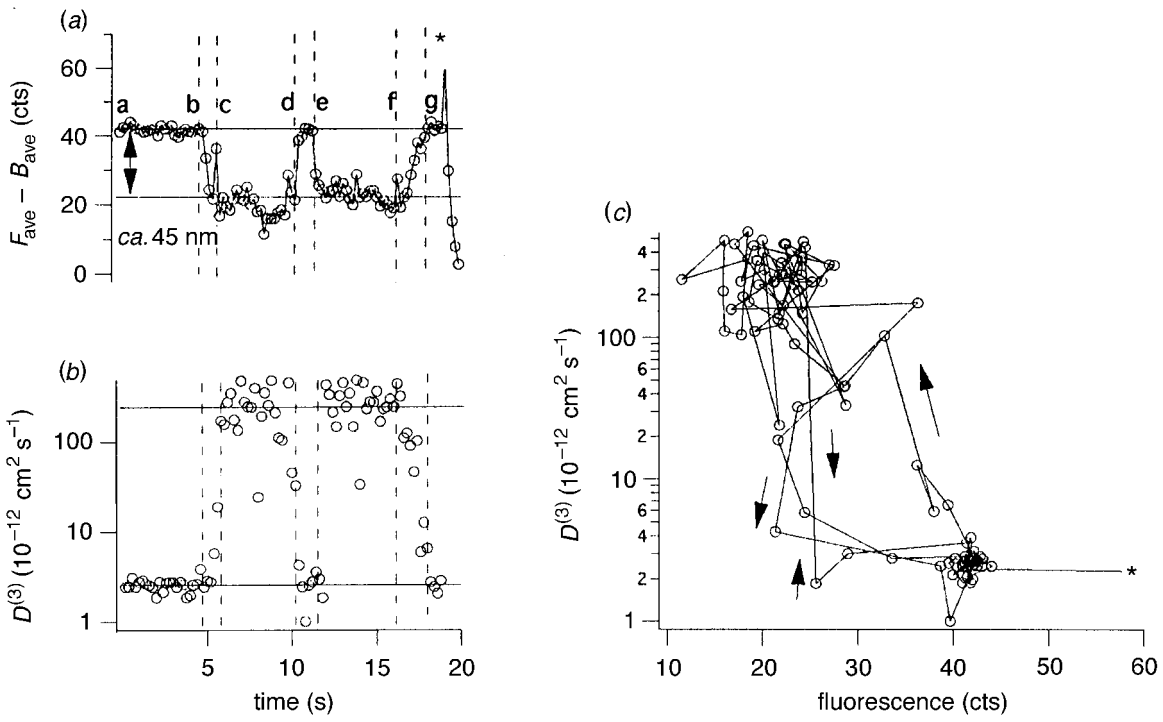

Figure 9. A vesicle undergoes reversible transitions between states. A vesicle was tracked over 20 s and its average fluorescence in the central 3×3 pixel region measured. The average fluorescence intensity was estimated as the rolling average over five frames (i.e. $F_n = \Sigma(F_{n-2} \ldots F_{n+2})/5$. The mean squared displacement (MSD) was now calculated at different times of the trajectory. Again, points $n-2$ to $n+2$ were used to calculate the value at point n. $D^{(3)}$ was determined from the $\Delta t \rightarrow 0$ approximation of the MSD vs Δt plot, see figure 10. (*a*) Average fluorescence over time. Stretches of the curve that were used to define 'states' are separated from phases of transition between states by dashed lines. The time of appearance of the cloud is indicated by an asterisk. Based on the *in vivo* calibration, the distance between the two steady-state levels of fluorescence is *ca.* 45 nm. (*b*) Plot of the average 3D diffusion coefficient over time. Time-scale as in (*a*). (*c*) The same data as in (*a*) and (*b*), now plotted parametrically as $\log[D^{(3)}(t)]$ versus $F(t)$. Points are clustered at two states.

8. EVANESCENT-WAVE MICROSCOPY MAKES IT POSSIBLE TO VISUALIZE SINGLE-VESICLE TRAJECTORIES

Due to the light-confinement of evanescent-wave excitation, photobleaching and phototoxic reactions are generally of minor concern when compared to conventional epi-excitation or confocal laser scanning microscopy. Therefore, evanescent-wave microscopy is ideal when long observation periods or time-resolved imaging at high frame-rates are desired. We have used the ability of TIRFM to resolve individual vesicles in a near-membrane slice together with the possibility of taking long image series to perform a detailed analysis of single-vesicle events based on 3D trajectories. Individual vesicles were characterized in terms of a 3D diffusion coefficient, $D^{(3)}$, derived from the slope of a plot of the mean squared displacement versus time for $\Delta t \rightarrow 0$ (Chandrasekhar 1943; Crank 1975; Kusumi *et al.* 1993; Saxton 1994), and their average fluorescence F, taken from a central 3 pixel $\times$ 3 pixel region of the spot. Both parameters were calculated as rolling average over stretches of the trajectory and pairs ($D^{(3)}$, F) were used to characterize states of vesicles as well as events that are consistent with transitions between states prior to fusion (figure 9). The states are defined biophysically in terms of particle mobility and average fluorescence. The dynamics of vesicles and transitions between states were explored at rest and after stimulation of exocytosis.

9. TRANSITIONS BETWEEN STATES

Vesicles were seen to change states. Vesicles had a lower mobility at the membrane (where their intensity was higher) when compared with deeper in the cytosol (figure 9). This decrease in mobility was seen both in lateral and axial direction. Vesicles were seen to stop their 'fast' movement (with $D^{(3)}$ in the order of 10^{-10} cm^2 s^{-1}) and their 3D diffusion coefficient decreased by almost two orders of magnitude (figure 9*b*). Some of the vesicles resumed their wandering later on. This was associated with a loss of fluorescence intensity and an increase of fluorescence fluctuations. In terms of the standard deviations of axial and lateral particle positions, vesicles near the membrane were on average 4.5 times less mobile in lateral direction and 3.7 times less mobile in axial direction than those in deeper regions of the cell (figures 10*a* and 11*c*). The trajectory of a single vesicle from the time of its appearance in the evanescent field to its disappearance, due to exocytosis, is shown on a plot of $D^{(3)}$ versus F (figure 9*c*). The vesicle entered the evanescent field and became brighter and lost its lateral mobility while it reached a stable maximum intensity at the same time. It is tempting to interpret these observations as the visualization of the

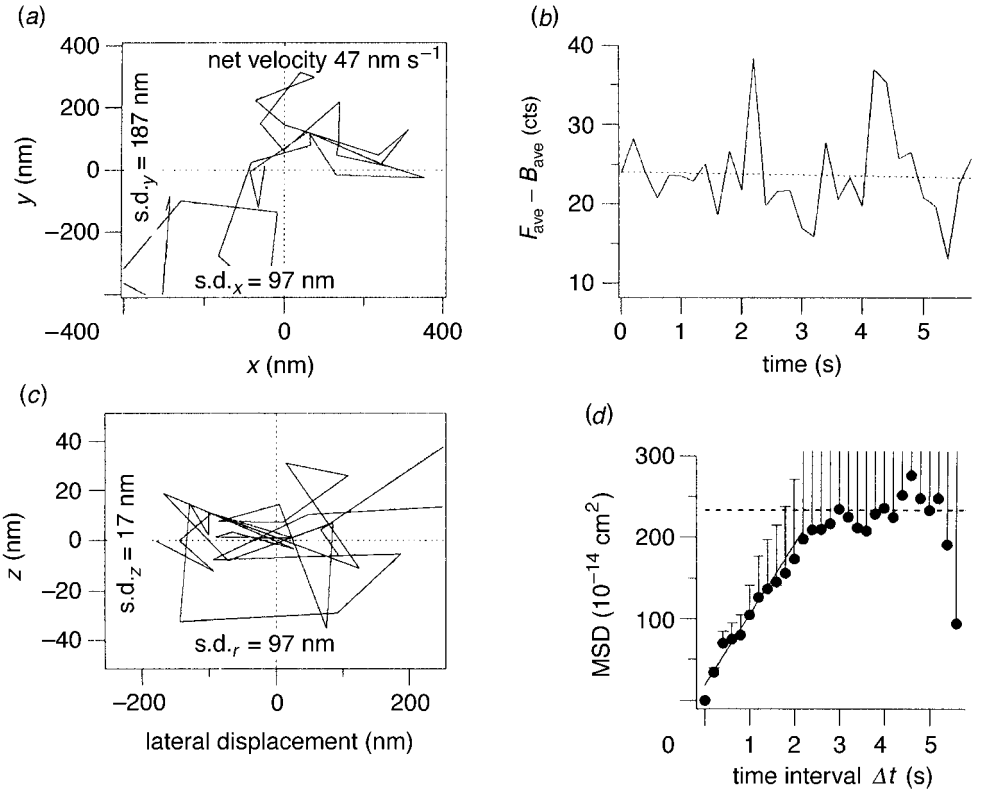

Figure 10. Trajectory of a mobile vesicle near the plasma membrane. (*a*) Lateral mobility of a vesicle, belonging to the mobile class V_1 on a plot of x versus y coordinates. Standard deviations are given with respect to the average position (0, 0) over the entire trajectory. (*b*) The fluorescence intensity, measured from a central 3 × 3 pixel region of the vesicle, over time was used to calculate the displacement in axial direction, $z = -d\ln(F/F_0)$, where F_0 is the intensity at $t=0$. (*c*) Lateral and axial particle movement were combined to yield the 3D trajectory, plotted as $r = \sqrt{\Delta x^2 + \Delta y^2}$ versus z. (*d*) The 3D diffusion coefficient was calculated from the $\Delta t \rightarrow 0$ asymptotic slope of the plot of the MSD versus time interval Δt of the trajectory. For this vesicle, $D^{(3)}$ was 3.21 ± 0.86 10^{-10} cm^2 s^{-1}. The plot displays a negative curvature, indicative of constrained diffusion (see Kusumi *et al.* (1993) for details). From the asymptote for $\Delta t \rightarrow \infty$, the radius of the 'cage', confining vesicle movement is determined to 505 ± 173 nm. During the time of observation, the vesicle covered a total path length of 4.25 μm.

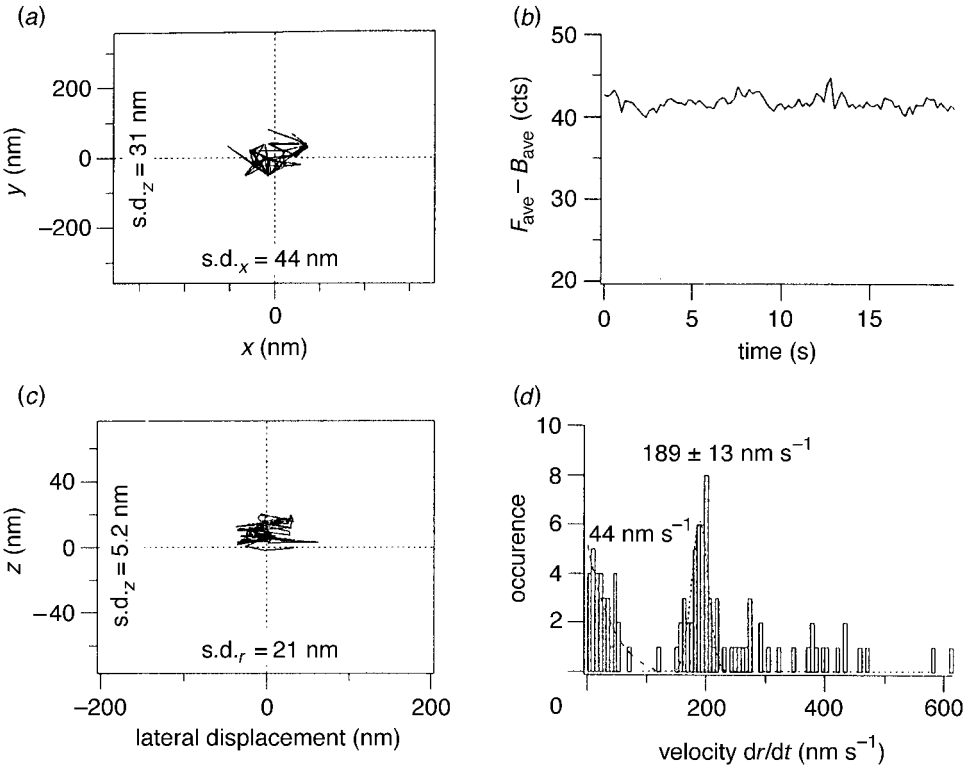

Figure 11. Example of an immobilized vesicle at the plasma membrane. (*a*) Lateral mobility on a plot of Δx versus Δy about the average position $(x, y) = (0, 0)$. (*b*) Fluorescence as a function of time, fluctuations are in the order of 2% (42 ± 0.8 counts, mean ± s.d.), corresponding to calculated axial jitters of ±2.5 nm, below the precision of our measurements. (*c*) Axial position z was calculated from the fluorescence fluctuations (*b*), relative to the position at $t=0$, z_0. Positions were averaged over the 20 s of the entire trajectory and the mean was subtracted. Standard deviations for axial and lateral directions are given in the graphs. (*d*) Histogram of velocities dr/dt of vesicle movement. Top speed is about 600 nm s^{-1}, the minimum below 1 nm s^{-1}. Velocities are distributed with a peak centred about 189 ± 13 nm s^{-1} (dotted line) and a slower movement with a mean of 44 nm s^{-1} (dashed line).

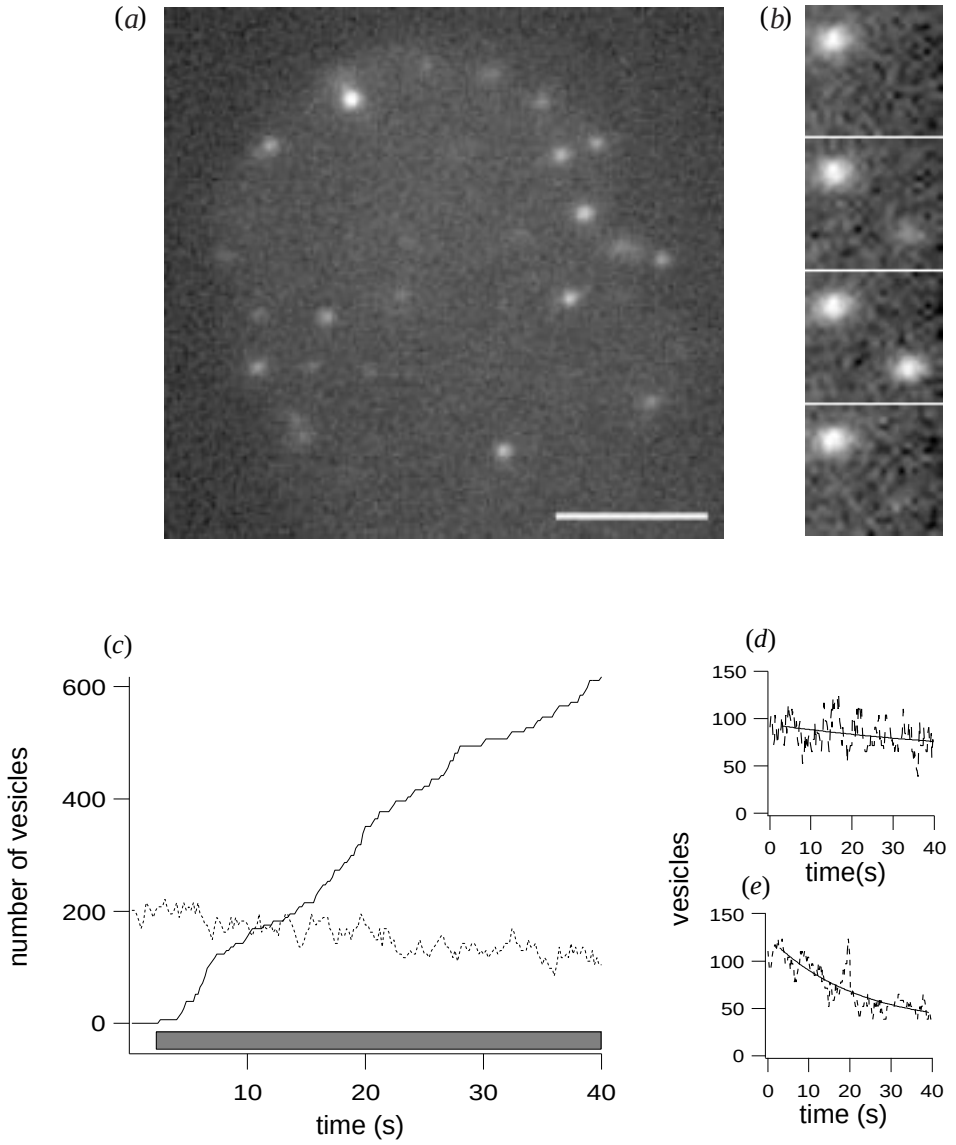

Figure 12. Pool dynamics. (*a*) Large dense-core vesicles are seen as fluorescent spots in the 'footprint' region of a chromaffin cell. The footprint diameter is *ca.* 14 μm (the scale bar indicates 5 μm). The angle of incidence was 70.0°, corresponding to a calculated penetration depth of the evanescent wave of 75 nm. Within *ca.* 110 nm, the vesicles' intensity decreased from its maximum to values that were indistinguishable from intracellular background. (*b*) Vesicles enter and leave the region of excitation even in the absence of stimulation. (*c*) In resting cells, about 30–34 vesicles are visible within the footprint region, corresponding to an average density of $0.21 \pm 0.03\ \mu m^{-2}$ or about 200 when scaled to the entire cell surface area. The total number of visible vesicles decreases only gradually after stimulation, indicating the supply of new vesicles to the observed region. The grey bar indicates the period of continuous local application of 60 mM K^+ from a puffer pipette. The solid trace represents the cumulative number of vesicles lost through exocytosis (pool 'E'). Secretion starts at $t = 2.6$ s, *ca.* 100 ms after K^+ application. (*d*) The number of highly mobile vesicles V_1 changes only after maintained stimulation and decays mono-exponentially with a time-constant of about 1 min, $\tau = 59.8$ s. (*e*) The average number of less mobile vesicles (V_2) decreases after stimulation with a time-constant of about 21 s. (Modified from Oheim *et al.* (1999).)

docking of the vesicle to its binding site at the plasma membrane. Tracking parameters were derived from stretches of the trajectory before and after 'docking'. The vesicle moved from the dimmer, high mobility class to the brighter, less mobile one (figure 9*c*) with several reversals in direction (arrows) before it finally disappeared after releasing its contents into the extracellular space (asterisk).

Fluorescence intensities and 3D diffusion coefficients that were obtained from the analysis of stretches of the trajectory (between the dashed lines on figure 9) are summarized in table 1.

10. VESICLES CAN BE GROUPED INTO TWO CLASSES

A striking feature when looking at time-resolved image stacks of cells in the absence of stimulation is that vesicles largely fall into two classes (figure 12*a*). Bright spots are seen to dwell at one place without displaying much activity, whereas other, dimmer vesicles are seen to move slowly while their intensity changes. A single-vesicle analysis—similar to that in figure 9 for many vesicles—reveals a stunning degree of complexity of vesicle dynamics near the plasma membrane. Most vesicles

Table 1. *Particle tracking parameters derived from different stretches of the curves in figure 9*

(The vesicle movement is interpreted as the reversible transition between two states of different fluorescence intensity and mobility. Ranges and abbreviations as on the graphs of figure 9.)

range	diffusion coefficient $D^{(3)}$ (10^{-10} cm^2 s^{-1})	average fluorescence F_0-B_0 (counts)
a–b	2.6±0.4	41.7±1.0
c–d	259.8±147.7	20.6±4.9
d–e	2.7±1.0	40.8±1.6
e–f	293.4±115.2	23.8±2.9
g–fusion of the vesicle	2.54±0.4	42.5±0.9

(>98%) belonged either to the dim mobile class (with a 3D diffusion coefficient of *ca.* 10^{-10} cm^2 s^{-1} and an average fluorescence of 23 cts above background (an example of which is shown in figure 10) or the brighter (42 cts) but markedly less mobile class with $D^{(3)} \approx 10^{-12}$ cm^2 s^{-1} (figure 12). Vesicles are seen to change states even in resting cells. On stimulation, only spots of the bright class underwent exocytosis (evidenced by the cloud of released dye molecules), while the dimmer vesicles have to join the bright pool of immobile vesicles first before becoming 'fusion competent'. Membrane depolarizations that evoke Ca^{2+}-entry through voltage-activated Ca^{2+}-channels result in a selective increase of the transitions leading towards exocytosis: both the rate of vesicles that came up in the evanescent field and the rate of 'docking' increased at elevated $[Ca^{2+}]_i$ (Oheim *et al.* 1999). In addition to mobile and immobilized vesicles there were some vesicles that displayed rapid flickers between the states and other vesicles that covered large distances during the time of observation. The results emphasize the importance of the reversibility of transitions prior to exocytosis.

11. POOL DYNAMICS

While the sizes of the two visible vesicle pools remained constant in the absence of stimulation (figure 12*c*, first 2 s), vesicles occasionally changed from the brighter, less mobile state V_1 to the dimmer, highly mobile state V_2, and vice versa, at a rate of 1.5 vesicles s^{-1}. (Rates are reported here as the number of vesicles undergoing a stated transition per second in the entire footprint region. To arrive at a whole-cell estimate, these numbers must be multiplied by a factor of 6 to 7). In addition, new vesicles spontaneously appeared or visible vesicles disappeared at equal rates of 7.1 vesicles s^{-1}, indicating a continuous exchange between vesicles that are visible and others in an invisible reserve pool—located deeper in the cell, beyond the reach of the evanescent field (figure 12*b*). For convenience, the pools of vesicles are referred to as V_1, V_2 and I, for vesicles that are dim and highly mobile, bright but less mobile and 'invisible', respectively. On exposure of chromaffin cells to extracellular solution containing 60 mM K^+ (figure 12*c*, grey bar), fluorescent spots disappeared in a cloud of released dye molecules. Spots that have disappeared will be referred to as vesicles accumulating in a pool E, for vesicles that have undergone exocytosis. In spite of the loss of vesicles, during the initial 15 s of maintained K^+ elevation, the total number of visible vesicles (pools V_1+V_2) remained almost constant (figure 12*c*, dashed line). This was due to the recruiting of new vesicles from the invisible reserve pool I. Although the rate of recruitment of new vesicles was enhanced on stimulation, the reverse rate remained approximately constant. The net effect of stimulation was that the pool of near-membrane vesicles was depleted at the expense of V_2 (with a time-constant of *ca.* 21 s, figure 12*e*), before maintained or repetitive depolarization caused the size of V_1 to decrease as well ($\tau \approx 1$ min, figure 12*d*).

12. CONCLUSION AND OUTLOOK

TIRFM not only constitutes an independent assay for pool depletion but opens a window to studying dynamics within the near-membrane pool of vesicles that had previously been hidden from the experimenter. TIRFM allows one to study aspects of secretion that have been inaccessible in living cells, in particular the spatial relations and dynamics of vesicles prior to and during exocytosis, and re-supply of the near-membrane pool of vesicles. With fluorophores other than acidophilic dyes (Lang *et al.* 1997; Miesenböck & Rothman 1997; Wacker *et al.* 1997; Miesenböck *et al.* 1998), TIRFM is the experimental tool to bridge the gap between existing assays for vesicle fusion on the one hand and biochemical studies of protein function on the other hand.

A variety of techniques for measuring exocytosis, endocytosis and vesicle recycling in living cells in almost real-time has resulted in a rapid expansion of the knowledge of these processes in neurons and neuroendocrine cells. Each technique has contributed unique and complementary information about the vesicle cycle, advancing our knowledge of the kinetics of fusion events, the identity of membrane proteins and the spatial patterns involved in vesicular exocytosis. Naturally, capacitance measurements, amperometry and optical methods have inherent limitations; some of these shortcomings are likely to be resolved by using more than one method simultaneously. Ever-more specific fluorophores, novel detection schemes and advances in digital image processing together have further extended our ability to image individual secretory granules and vesicles in living cells so that studying single-vesicle events in neurons has come within reach.

The authors would like to acknowledge the support of the Nuffield Foundation, the Wellcome Trust and the Royal Society to R.H.C. This work was supported by a British Council Academic Research Collaboration grant to W.S. and R.C.H. M.O. is the holder of a University of Edinburgh graduate studentship grant.

REFERENCES

Agard, D. A., Hiraoka, Y., Shaw, P. & Sedat, J. W. 1989 Fluorescence microscopy in three dimensions. *Meth. Cell Biol.* **30**, 353–377.

Albillos, A., Dernick, G., Horstmann, H., Almers, W., Alvares de Toledo, G. & Lindau, M. 1997 The exocytotic event in chromaffin cells revealed by patch amperometry. *Nature* **389**, 509–512.

Almers, W. 1990 Exocytosis. *A. Rev. Physiol.* **52**, 607–624.

Ammäla, C., Ashcroft, F. & Rorsiian, P. 1993 Calcium-independent potentiation of insulin release by cyclic AMP in single beta-cells. *Nature* **363**, 365–368.

Angleson, J. K. & Betz, W. J. 1997 Monitoring secretion in real time: capacitance, amperometry and fluorescence compared. *TINS* **20**, 281–287.

Augustine, G. J. & Neher, E. 1992 Calcium requirements for secretion in bovine chromaffin cells. *J. Physiol.* **450**, 247–271.

Axelrod, D. 1981 Cell–substrate contacts illuminated by TIRF. *J. Cell Biol.* **89**, 141–145.

Axelrod, D., Hellen, E. H. & Fulbright, R. M. 1992 Total internal reflection fluorescence. In *Topics in fluorescence spectroscopy*, vol. 3 (ed. J. R. Lakovicz), p. 289. New York: Plenum Press.

Betz, W. J. 1970 Depression of transmitter release at the neuromuscular junction of the frog. *J. Physiol.* **206**, 629.

Betz, W. J. & Angleson, J. K. 1997 Cellular secretion: now you see it, now you don't. *Nature* **388**, 423–424.

Betz, W. J. & Bewick, G. S. 1992 Optical analysis of synaptic vesicle recycling at the frog neuromuscular junction. *Science* **255**, 200–203.

Betz, W. J., Mao, F. & Bewick, G. S. 1992 Activity-dependent fluorescence staining and destaining of living vertebrate motor nerve terminals. *J. Neurosci.* **12**, 363–375.

Betz, W. J., Mao, F. & Smith, C. B. 1996 Imaging exocytosis and endocytosis. *Curr. Opin. Neurobiol.* **6**, 365–371.

Biggley, W. H., Lloyd, J. E. & Selinger, H. H. 1967 The spectral distribution of firefly light. II. *J. Gen. Physiol.* **50**, 1681–1692.

Bittner, M. A. & Holz, R. W. 1992 A temperature-sensitive step in exocytosis. *J. Biol. Chem.* **267**, 16 226–16 229.

Born, M. & Wolf, E. 1980 *Principles of optics*. Oxford: Pergamon Press.

Burghardt, T. P. & Thompson, N. L. 1984*a* Effect of planar dielectric interfaces on fluorescence emission and detection: evanescent excitation with high aperture observation. *Biophys. J.* **46**, 729–739.

Burghardt, T. P. & Thompson, N. L. 1984*b* Evanescent intensity of a focused Gaussian light beam undergoing total internal reflection in a prism. *Opt. Eng.* **23**, 62–67.

Burke, N. V., Han, W., Li, D., Takimoto, K., Watkins, S. C. & Levitan, E. S. 1997 Neuronal peptide release is limited by secretory granule movement. *Neuron* **19**, 1095–1102.

Burmeister, J. S., Truskey, G. A. & Reichert, W. M. 1994 Quantitative analysis of variable-angle total internal reflection fluorescence microscopy (VA-TIRFM) of cell–substrate contacts. *J. Microsc.* **173**, 39–51.

Chandrasekhar, S. 1943 Stochastic problems in physics and astronomy. *Rev. Mod. Phys.* **15**, 18–89.

Chiu, M. H., Lee, J. Y. & Su, D. C. 1997 Refractive-index measurement based on the effects of total internal-reflection and the uses of heterodyne interferometry. *Appl. Opt.* **36**, 2936–2939.

Chow, R. H., Rüden, L. v. & Neher, E. 1992 Delay in vesicle fusion revealed by electrochemical monitoring of single secretory events in adrenal chromaffin cells. *Nature* **356**, 60–63.

Conibear, P. B. & Bagshaw, C. R. 1996 Measurement of nucleotide exchange kinetics with isolated synthetic myosin fibres using flash photolysis. *FEBS Lett.* **380**, 13–16.

Crank, J. 1975 *The mathematics of diffusion*. Oxford: Clarendon Press.

Curtis, A. S. G. 1964 The mechanism of cell adhesion to glass, a study by interference reflection microscopy. *J. Cell Biol.* **20**, 199.

DelCastillo, J. & Katz, B. 1954 Quantal components of the end-plate potential. *J. Physiol.* **124**, 560–573.

Denk, W., Strickler, J. H. & Webb, W. W. 1990 Two-photon laser scanning fluorescence microscopy. *Science* **248**, 73–76.

Denk, W., Yuste, R., Svoboda, K. & Tank, D. W. 1996 Imaging calcium dynamics in dendritic spines. *Curr. Opin. Neurobiol.* **6**, 372–378.

Diwu, Z., Zhang, Y. Z. & Haugland, R. P. 1994 Novel site-selective fluorescent probes for lysosome and acididic organelle staining and long-term tracking. *Cytometry* **7**, 77. (Suppl.)

Elmquist, D. & Quastel, D. M. J. 1965 A quantitative study of end-plate potentials in isolated human muscle. *J. Physiol.* **178**, 505–529.

Farinas, J., Simanek, V. & Verkman, A. S. 1995 Cell volume measured by total internal reflection microfluorimetry: application to water and solute transport in cells transfected with water channel homologs. *Biophys. J.* **68**, 1613–1620.

Gillis, K. D. 1994 Techniques for membrane capacitance measurements. In *Single channel recording* (ed. B. Sakmann & E. Neher). New York: Plenum.

Gillis, K. D. & Chow, R. H. 1997 Kinetics of exocytosis in adrenal chromaffin cells. *Cell Dev. Biol.* **8**, 133–140.

Gillis, K. & Misler, S. 1993 Enhancers of cytosolic cAMP augment depolarization-induced exocytosis from pancreatic B-cells: evidence for effects distal to Ca^{2+} entry. *Pflügers Archiv. Eur. J. Physiol.* **424**, 195–197.

Gillis, K. D., Mössner, R. & Neher, E. 1996 Protein kinase C enhances exocytosis from chromaffin cells by increasing the size of the readily releasable pool of secretory granules. *Neuron* **16**, 1209–1220.

Gingell, D. & Todd, I. 1979 Interference reflection microscopy. A quantitative theory for image interpretation and its application to cell–substratum separation measurement. *Biophys. J.* **26**, 507–526.

Gingell, D., Todd, I. & Bailey, J. 1985 Topography of cell–glass apposition revealed by total internal reflection fluorescence of volume markers. *J. Cell Biol.* **100**, 1334–1338.

Gingell, D., Heavens, O. S. & Mellor, J. S. 1987 General electromagnetic theory of total internal reflection fluorescence: the quantitative basis for mapping cell–substratum topography. *J. Cell Sci.* **87**, 677–693.

Hamill, O. P., Marty, A., Neher, E., Sakmann, B. & Sigworth, F. 1981 Improved patch-clamp techniques for high-resolution current recording from cells and cell-free membrane patches. *Pflügers Arch. Eur. J. Physiol.* **391**, 85–100.

Henkel, A. W. 1998 Capacitance steps recorded from chromaffin cells and red blood cells (RBC). *Biophys. J.* **74**, A97.

Hiraoka, Y., Sedat, J. W. & Agard, D. A. 1990 Determination of the three-dimensional imaging properties of a light microsope system—partial confocal behaviour in epifluorescence microscopy. *Biophys. J.* **57**, 325–333.

Horrigan, F. T. & Bookman, R. J. 1994 Releasable pools and the kinetics of exocytosis in chromaffin cells. *Neuron* **13**, 1119–1129.

Kaether, C. & Gerdes, H. H. 1995 Visualization of protein transport along the decretory pathway using green fluorescent protein. *FEBS Lett.* **369**, 267–271.

Kusumi, A., Sako, Y. & Yamamoto, M. 1993 Confined lateral diffusion of membrane receptors as studied by single particle tracking (Nanovid microscopy). Effects of calcium-induced differentiation in cultured epithelial cells. *Biophys. J.* **65**, 2021–2040.

Lang, T., Wacker, I., Steyer, J., Kaether, C., Wunderlich, I., Suldati, T., Gerdes, H. H. & Almers, W. 1997 Ca^{2+}-triggered peptide secretion in single cells imaged with green fluorescent protein and evanescent-wave microscopy. *Neuron* **18**, 857–863.

Lanni, F., Waggoner, A. S. & Taylor, D. L. 1985 Structural organization of interphase 3T3 fibroblasts studied by TIRFM. *J. Cell Biol.* **100**, 1091–1102.

Li, H. & Xie, S. S. 1996 Measurement method of the refractive-index of biotissue by total internal-reflection. *Appl. Opt.* **35**, 1793–1795.

Lipp, P. & Niggli, E. 1993 Ratiometric confocal Ca^{2+}-measurements with visible wavelength indicators in isolated cardiac myocytes. *Cell Calcium* **14**, 359–372.

Maiti, S., Shear, J. B., Williams, R. M., Zipecl, W. R. & Webb, W. W. 1997 Measuring serotonin distribution in live cells with three-photon excitation. *Science* **275**, 530–532.

Miesenböck, G. & Rothman, J. E. 1997 Patterns of synaptic activity in neuronal networks recorded by light emission from synaptolucins. *Proc. Natl Acad. Sci. USA* **94**, 3402–3407.

Miesenböck, G., DeAngelis, D. A. & Rothman, J. E. 1998 Visualizing secretion and synaptic transmission with pH-sensitive green fluorescent proteins. *Nature* **394**, 192–195.

Minsky, M. 1961 *Microscopy apparatus.* (Submitted 1957.) US patent no. 3013467 USA.

Minsky, M. 1988 Memoir on inventing the confocal scanning microscope. *Scanning* **10**, 128–138.

Moser, T. & Neher, E. 1996 Rapid exocytosis in single chromaffin cells recorded from adrenal slices. *Biophys. J.* **70**, SU306–U306.

Neher, E. 1998 Vesicle pools and Ca^{2+} microdomains: new tools for understanding their roles in neurotransmitter release. *Neuron* **20**, 389–399.

Neher, E. & Marty, A. 1982 Discrete changes in of cell membrane capacitance observed under conditions of enhanced secretion in bovine adrenal chromaffin cells. *Proc. Natl Acad. Sci. USA* **79**, 6712–6716.

Neher, E., Llano, I., Hopt, A., Würriehausen, F. & Tan, Y. 1998 Fast scanning and efficient photodetection in a simple two photon microscope. *Biophys. J.* **74**, A184.

Oheim, M., Loerke, D., Stühmer, W. & Chow, R. H. 1998*a* The last few milliseconds in the life of a secretory granule. Docking, dynamics and fusion visualized by total internal reflection fluorescence microscopy (TIRFM). *Eur. Biophys. J.* **27**, 83–98.

Oheim, M., Loerke, D., Preitz, B. & Stühmer, W. 1998*b* A simple optical configuration for depth-resolved imaging using variable-angle evanescent-wave microscopy. *Proc. Eur. Opt. Soc.* **3568**, 1–10.

Oheim, M., Loerke, D., Chow, R. H. & Stühmer, W. 1998*c* Quantitative variable-angle total internal reflection fluorescence microscopy (VA-TIRFM) visualises dynamics of chromaffin granules with nanometer axial resolution. *Biophys. J.* **74**, A96.

Oheim, M., Loerke, D., Stühmer, W. & Chow, R. H. 1999 Multiple stimulation-dependent processes regulate the size of the releasable pool of vesicles. *Eur. Biophys. J.* **28**, 91–101.

Ölveczky, B. P., Periasamy, N. & Verkman, A. S. 1997 Mapping fluorphore distributions in 3 dimensions by quantitative multi-angle total internal reflection fluorescence microscopy (MA-TIRFM). *Biophys. J.* **72**, A212.

Pawley, J. B. 1995 *Handbook of biological confocal microscopy.* New York, London: Plenum.

Piston, D. W., Kirby, M. S., Cheng, H., Lederer, W. J. & Webb, W. W. 1994 Two-photon-excitation fluorescence imaging of three-dimensional calcium-ion activity. *Appl. Opt.* **33**, 662–669.

Reichert, W. M. & Truskey, G. A. 1990 Total internal reflection fluorescence (TIRF) microscopy. 1. Modelling cell contact region fluorescence. *J. Cell Sci.* **96**, 219–230.

Reichert, W. M., Suci, P. A., Ives, J. T. & Andrade, J. D. 1987 Evanescent detection of adsorbed protein concentration–distance profiles: fit of simple models to variable-angle total internal reflection fluorescence data. *Appl. Spec.* **41**, 503–508.

Rojas, E., Forsberg, E. & Pollard, H. B. 1986 Optical detection of calcium dependent ATP release from stimulated medullary chromaffin cells. *Adv. Exp. Med. Biol.* **211**, 7–29.

Rojas, E., Cena, V., Stutzin, A., Forsberg, E. & Pollard, H. B. 1990 Characteristics of receptor-operated and membrane potential-dependent ATP decretion from adrenal medullary chromaffin cells. In *Biological actions of extracellular ATP*, vol. 603 (ed. G. R. Dubyak & J. S. Fedan), pp. 311–323. New York Academy of Sciences.

Rosenmund, C. & Stevens, C. F. 1996 Definition of the readily releasable pool of vesicles at hippocampal synapses. *Neuron* **16**, 1197–1207.

Rüden, L. v. & Neher, E. 1993 A Ca-dependent early step in the release of catecholamines from adrenal chromaffin cells. *Science* **262**, 1061–1065.

Ryan, T. A., Reuter, H. & Smith, S. J. 1997 Optical detection of quantal presynaptic membrane turnover. *Nature* **388**, 478–482.

Saxton, M. J. 1994 Anomalous diffusion due to obstacles: a Monte-Carlo study. *Biophys. J.* **66**, 394–401.

Smith, C. B. & Betz, W. J. 1996 Simultaneous independent measurement of endocytosis and exocytosis. *Nature* **380**, 531–534.

Smith, C., Moser, T., Xu, T. & Neher, E. 1998 Cytosolic Ca^{2+} acts by two separate pathways to modulate the supply of release-competent vesicles in chromaffin cells. *Neuron* **20**, 1243–1253.

Stevens, C. F. & Tsujimoto, T. 1995 Estimates for the pool size of releasable quanta at a single central synapse and for the time required to refill the pool. *Proc. Natl Acad. Sci. USA* **92**, 846–849.

Steyer, J. A., Horstmann, H. & Almers, W. 1997 Transport, docking and exocytosis of single secretory granules in live chromaffin cells. *Nature* **388**, 474–478.

Stout, A. L. & Axelrod, D. 1989 Evanescent field excitation of fluorescence by epi-illumination microscopy. *Appl. Opt.* **28**, 5237–5242.

Suci, P. & Reichert, W. M. 1988 Determination of fluorescence density profiles of Langmuir-Blodgett-deposited films by analysis of variable-angle fluorescence data curves. *Langmuir* **1988**, 1131–1141.

Svoboda, K., Denk, W., Knox, W. H. & Tsuda, S. 1996 2-photon-excitation scanning microscopy of living neurons with a saturable bragg reflector mode-locked diode-pumped cr-lisralfl laser. *Opt. Lett.* **21**, 1411–1413.

Swaminathan, R., Bicknese, S., Periasamy, N. & Verkman, A. S. 1996 Cytoplasmic viscosity near the cell plasma-membrane—translational diffusion of a small fluorescent solute measured by total internal reflection-fluorescence photobleaching recovery. *Biophys. J.* **71**, 1140–1151.

Terakawa, S., Fan, J. H., Kumakura, K. & Ohara-Imaizumi, M. 1991 Quantitative analysis of exocytosis directly visualised in living chromaffin cells. *Neurosci. Lett.* **12**, 82–86.

Truskey, G. A., Burmeister, J. S., Grapa, E. & Reichert, W. M. 1992 Total internal reflection fluorescence microscopy (TIRFM). II. Topographical mapping of relative cell–substrate separation distances. *J. Cell Sci.* **103**, 491–499.

Wacker, I., Kaether, C., Kroemer, A., Migula, A., Almers, W. & Gerdes, H. H. 1997 Microtubule-dependent transport of secretory vesicles visualized in real-time with a gfp-tagged secretory protein. *J. Cell Sci.* **110**, 1453–1463.

Wall, J. E., Buijs-Wilts, M., Arnold, J. T., Wang, W., White, M. W., Jennings, L. K. & Jackson, C. W. 1994 A flow cytometric assay using mepacrine for study of uptake and release of platelet dense granule contents. *Br. J. Haematol.* **89**, 380–385.

Wightman, R. M., Jankowski, J. A., Kennedy, R. T., Kawagoe, K. T., Schroeder, T. J., Leszczszyn, F. J., Near, J. A., Diliberto, E. J. Jr & Viveros, O. H. 1991 Temporarily resolved catecholamine spikes correspond to single vesicle release from individual chromaffin granules. *Proc. Natl Acad. Sci. USA* **88**, 10 754–10 758.

Zhang, Y. Z. 1994 Novel fluorescent acidic organelle-sensitive dyes and mitochondrion-selective dyes that are well retained during cell fixation and permeabilization. *Mol. Biol. Cell* **5**, 113a.